Volume 4 | Number 5 | May 2020

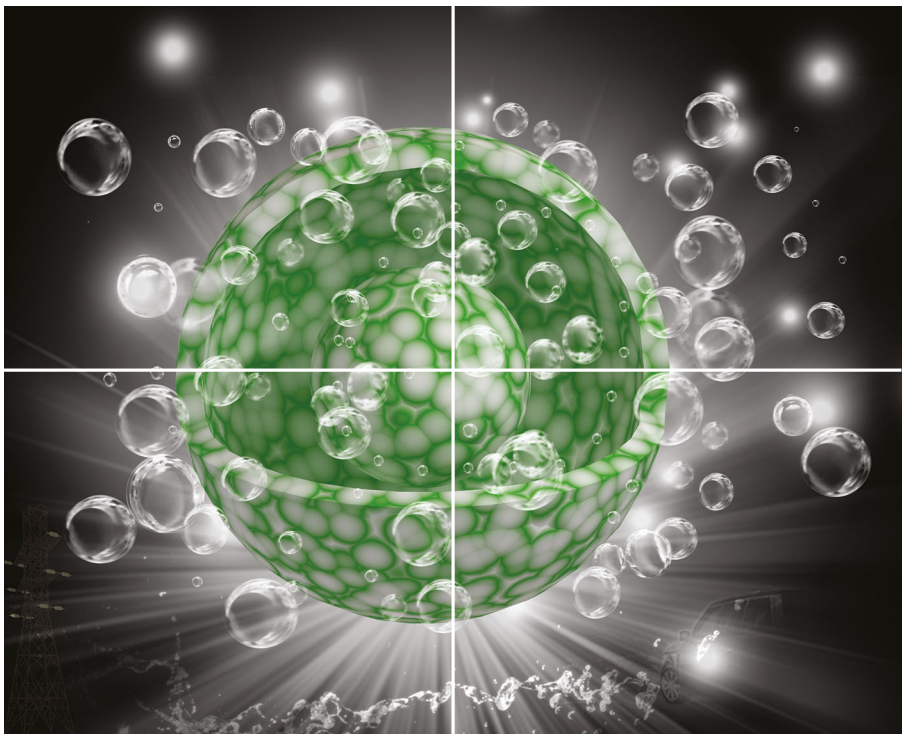

MATERIALS CHEMISTRY

FRONTIERS

CCS 中国化学会 CHINESE CHEMICAL SOCIETY

ICCAS 1956

ROYAL SOCIETY OF CHEMISTRY

rsc.li/frontiers-materials

MATERIALS CHEMISTRY FRONTIERS

RESEARCH ARTICLE

View Article Online
View Journal | View Issue

Cite this: *Mater. Chem. Front.*, 2020, **4**, 1366

Design and construction of bi-metal MOF-derived yolk–shell Ni_2P/ZnP_2 hollow microspheres for efficient electrocatalytic oxygen evolution†

Jinyang Zhang, Xuan Sun, Yang Liu, Linrui Hou and Changzhou Yuan *

Received 2nd March 2020,
Accepted 31st March 2020

DOI: 10.1039/d0qm00128g

rsc.li/frontiers-materials

It is highly challengeable to explore and design high-performance non-noble metal electrocatalysts for the oxygen evolution reaction (OER) towards highly efficient water electrolysis. Herein, we design and synthesize, for the first time, a novel cost-efficient electrocatalyst, *i.e.*, hierarchical yolk–shell Ni_2P/ZnP_2 hollow microspheres (NZP HMSs), *via* a two-step strategy involving a solvothermal process and subsequent phosphatization. When utilized as a promising electrocatalyst for the OER, the yolk–shell NZP HMS specimen exhibits more exceptional OER performances than its solid Ni_2P counterpart, including a lower overpotential of 210 mV at 10 mA cm^{-2}, a smaller Tafel slope of 57.8 mV dec^{-1} and more superior electrochemical stability in 1 M KOH. The superb electrocatalytic OER properties are attributed to the synergistic contributions from the Ni_2P/ZnP_2 hetero-interface at the nanoscale, favorable electronic conductivity and high electroactive surface area. More significantly, we strongly envision that this simple synthetic methodology can be highly versatile for other hierarchical yolk–shell hollow phosphides towards the OER and beyond.

1. Introduction

With the increasing demands of human society, non-renewable energy resources are gradually exhausted. As a consequence, electrochemical water splitting provides a good alternative for an efficient conversion of water into sustainable chemicals and fuels with renewable electricity, including both the cathodic hydrogen evolution reaction (HER) and the anodic oxygen evolution reaction (OER).[1–4] In particular, the OER generally suffers from a bottleneck, *i.e.*, a four-electron proton-coupled process, which results in its sluggish kinetics[5] and a substantially high activation energy barrier (namely, higher overpotential) based on the theoretical decomposition voltage of water (1.23 V, *vs.* RHE).[6]

Up to now, the state-of-the-art Ir-/Ru-based oxides have exhibited excellent OER performance with smaller overpotentials, *i.e.*, ~312 mV for IrO_2 and ~350 mV for RuO_2, for attaining a current density of 10 mA cm^{-2} and superior catalytic stability.[7,8] However, the high cost and scarcity of noble metals limit their practical utilization.[9] Therefore, development of earth-abundant, non-noble OER catalysts with desirable electrocatalytic performances for practical applications is of great significance.

In recent years, various transition metal (TM) phosphides,[10] oxides,[11] chalcogenides,[12] borides,[13] nitrides[14] and their composites[15] have emerged as effective OER catalysts. Among these cost-efficient catalysts, TM phosphides are regarded as catalysts with superior electrocatalytic activity and stability in alkaline media to effectively promote the OER process in terms of thermodynamics and kinetics. Moreover, from the view of catalyst structure, the number of active centers, as a momentous factor, must be taken into consideration for any electrocatalyst to render remarkable OER performance.[4] To this end, two effective strategies, *i.e.*, construction of three dimensional (3D) hierarchical porous (particularly hollow architectures) and multi-component hetero-interfaces, have been proposed.[16–19] Concretely, the former can maximally expose active edge sites on the catalyst surface. The latter can effectively reduce the chemisorption free energy of OH^-, promote the desorption of the intermediates from active centers, bring strong synergistic effects, and even increase the number of active centers.[18] For instance, 3D Fe_2O_3@Ni_2P/$Ni(PO_3)_2$/nickel foam (NF) achieved a current density of 10 mA cm^{-2} with a low overpotential of 177 mV.[16] 3D FeP@Ni_2P/NF only needed an overpotential of 290 mV to reach a current density of 50 mA cm^{-2} in 1 M KOH.[17] 3D $NiSe_2$–Ni_2P/NF merely required an ultralow overpotential of 220 mV to reach a current density of 50 mA cm^{-2}.[19] Therefore, the purposeful design of 3D hierarchical hollow structures has a direct effect on the electrochemical performance.[20–25] However, it is highly challengeable to develop a simple but efficient methodology to

School of Materials Science and Engineering, University of Jinan, Jinan 250022, P. R. China. E-mail: mse_yuancz@ujn.edu.cn, ayuancz@163.com

† Electronic supplementary information (ESI) available. See DOI: 10.1039/d0qm00128g

fabricate hierarchical hollow TM phosphides with hetero-interfaces at the nanoscale as highly efficient OER catalysts.

In this work, we firstly synthesized hierarchical yolk–shell Ni_2P/ZnP_2 hollow microspheres (NZP HMSs) *via* a facile low-temperature phosphatization of a bimetallic (Ni, Zn) organic framework precursor, and further investigated their OER performances in 1 M KOH electrolyte as an electrocatalyst. When evaluated as a competitive catalyst for the OER, the resultant yolk–shell NZP HMSs displayed excellent OER performance with a low overpotential of 210 mV at a current density of 10 mA cm^{-2} and a small Tafel slope of 57.8 mV dec^{-1} as well as excellent electrochemical stability, benefiting from the concerted contributions from their large electroactive surface, nanoscale Ni_2P/ZnP_2 hetero-interface and exceptional electrical conductivity.

2. Experimental section

2.1 Chemicals

All chemicals including $Ni(NO_3)_2{\cdot}6H_2O$, $Zn(NO_3)_2{\cdot}6H_2O$, dimethylformamide (DMF), 1,3,5-benzene tricarboxylic acid (BTC), polyvinylpyrrolidone (PVP), absolute alcohol and NaH_2PO_2 were purchased from Sinopharm Chemical Reagent Co. Ltd, and used as received without further purification. All aqueous solutions were freshly prepared by using high-purity water (18.25 MΩ cm^{-1} resistance).

2.2 Synthesis of yolk–shell NZP HMSs

Typically, 215 mg of $Ni(NO_3)_2{\cdot}6H_2O$, 215 mg of $Zn(NO_3)_2{\cdot}6H_2O$, and 140 mg of BTC were dissolved in 30 mL of DMF under magnetic stirring for 30 min. Then, the mixture was sealed in a 50 mL Teflon-lined autoclave and maintained at 150 °C for 6 h. After being cooled down to room temperature (RT) naturally, a green precipitate was separated by centrifugation, washed with DMF and absolute alcohol several times, dried in a vacuum oven at 60 °C overnight, and denoted as pre-NZP. Then, pre-NZP (100 mg) was mixed well with 300 mg of NaH_2PO_2. The mixture was further annealed at 600 °C for 2 h at a ramp rate of 3 °C min^{-1} under a N_2 atmosphere. After washing the mixture with 0.5 M HCl and water, and drying at 80 °C, yolk–shell NZP HMSs were obtained. For comparison, solid Ni_2P microspheres (NP MSs) were prepared as well but using 430 mg of $Ni(NO_3)_2{\cdot}6H_2O$ instead. The yolk–shell Ni_2P/ZnP_2 hollow microspheres (NZP-5 HMSs) were prepared by changing the ramp rate to 5 °C min^{-1}. The solid Ni_2P/ZnP_2 microspheres (NZP MSs) were produced by using $Ni(NO_3)_2{\cdot}6H_2O$ (280 mg) and $Zn(NO_3)_2{\cdot}6H_2O$ (150 mg). The yolk–shell Ni_2P hollow microspheres (NP HMSs) were obtained with 15 mL of DMF and 15 mL of absolute alcohol instead of 30 mL of DMF. And the $Zn_3(PO_4)_2$ hollow microspheres (ZOP HMSs) were obtained without the addition of Ni species. One especially notes that other synthetic parameters for all the above products were kept the same as those of yolk–shell NZP HMSs. And the precursor for the solid NP MSs was designed as pre-NP for convenience.

2.3 Material characterization

Morphologies of the samples were investigated with a field-emission scanning electron microscope (FESEM, JEOL-6300F), a transmission electron microscope (TEM) and a high-resolution TEM (HRTEM, TECNAI-20) system equipped with an energy dispersive X-ray (EDX) analysis setup (Genesis XM2). The X-ray diffraction (XRD) patterns of the products were recorded with a Bruker D8 Focus Diffraction System using a Cu Kα source (λ = 0.15406 nm). Nitrogen adsorption–desorption tests were determined on a surface area analyzer (TriStar II 3020) at 77 K. The mesopore and micropore size distributions were derived by the Barrett–Joyner–Halenda (BJH) and density functional theory (DFT) methods, respectively. X-ray photoelectron spectroscopy (XPS) measurements were performed on a photoelectron spectrometer using Al Kα radiation as the excitation source (a VGESCALAB MKII X-ray photoelectron). All the peaks were calibrated with the C 1s spectrum at a binding energy of 284.8 eV. Thermogravimetric and differential scanning calorimetry (TG-DSC) analyses were performed on a STA449 F5 (NETZSCH, Germany).

2.4 Electrochemical measurements

The catalyst suspension was prepared from a solution (1 mL) consisting of 2.5 mg of catalyst, 100 μL of Nafion and 900 μL of ethanol. A Ni foam (porosity 95% and purity 95%) was pretreated and then used as a catalyst support. Specifically, the purchased NF was immersed in 12 M HCl for 10 min, then rinsed well with water, and finally, cut for determining the geometric surface area. The remaining surface was isolated from the electrolyte using hot glue as the insulator to ensure an exposed surface area of 1.0 cm^2 for subsequent electrochemical tests. Electrochemical measurements were carried out in a standard three-compartment electrochemical cell consisting of a working electrode, a Pt counter electrode, and an Ag/AgCl (saturated KCl aqueous solution) reference electrode on an IVIUM electrochemical workstation (Netherlands).

The catalyst was typically loaded on the pretreated NF *via* drop-casting 40 μL of the catalyst ink, equivalent to a loading of 0.1 mg cm^{-2}. The electrochemical OER experiments over the solid NP MSs and yolk–shell NZP HMSs were conducted in 250 mL of 1 M KOH aqueous solution (pH = 13.6). Before the OER test, the NF was first activated with 100 cyclic voltammetry (CV) sweeps at a scan rate of 100 mV s^{-1}. Linear sweep voltammetry (LSV) curves were produced at a scan rate of 5 mV s^{-1} across a potential window of 1.20–1.75 V (*vs.* reversible hydrogen electrode, RHE) without *iR* compensation. The cycle stability of the yolk–shell NZP HMSs was evaluated by a long-term durability test at 1.44 V (*vs.* RHE). Electrochemical impedance spectroscopy (EIS) was performed in the frequency range from 100 kHz to 0.01 Hz with an AC signal amplitude of 5 mV at 1.44 V (*vs.* RHE). During electrochemical experiments, the electrolyte was always agitated using a magnetic stirrer rotating at 350 rpm at room temperature (RT, 25 °C).

The current density was normalized over the geometric surface area of the electrode. The Ag/AgCl electrode was calibrated to

1.001 ± 0.002 V *vs.* RHE in a standard three-electrode system: the Ag/AgCl electrode as the reference electrode and two polished Pt plates as the working and counter electrodes in H_2-saturated 1 M KOH solution.[26] All potentials measured were calibrated to the RHE using the following eqn (1):

$$E_{RHE} = E_{Ag/AgCl} + 0.197 + 0.0591 \times pH \quad (1)$$

The electrochemical active surface area (EASA) was evaluated in terms of double layer capacitance (C_{dl}), assuming a C_{dl} capacitance of 60 μF cm^{-2}.[27] The CV scans were performed at different scan rates within a potential window of 0.1 V, where no faradaic process occurred. The CV scanning sequence was in the order of 20, 40, 60, 80, 100 and 120 mV s^{-1}. The turnover frequency (TOF) values were calculated by the following equation:[28]

$$TOF = \frac{jA}{4nF} \quad (2)$$

where j is the current density (mA cm^{-2}) at an overpotential of 210 mV, A is the geometric surface area of the Ni foam electrode (cm^2), number 4 means four electrons per mole of O_2, F is the Faraday constant (96 485 C mol^{-1}), and n is the number (mole) of active sites in the working electrode. Herein, the Ni species was only regarded as the active site, so the Zn and P atoms were ignored when calculating the TOF values of the solid NP MSs and yolk–shell NZP HMSs.

3. Results and discussion

3.1 Physicochemical and structural characteristics of yolk–shell NZP HMSs

In this work, a two-step synthetic strategy, *i.e.*, a hydrothermal process followed by high-temperature phosphatization in a nitrogen atmosphere, is adopted, as described in Fig. 1a. Typically, the Ni-based benzotriacetic acid framework precursor (*i.e.*, pre-NP) and Ni/Zn-MOF precursor (*i.e.*, pre-NZP) are obtained *via* a surfactant-mediated hydrothermal treatment at 150 °C.[29] Apparently, both precursors exist with a similar solid microspherical structure of size ~1 μm (Fig. S1, ESI†). During the subsequent calcination, three endothermic peaks, corresponding to the loss of adsorbed/bound water (P1, 100 °C), decomposition of PVP (P2, 420 °C) and sublimation of Zn (P3, 700 °C), respectively, are distinct in the thermogravimetric and differential scanning calorimetry (TG-DSC) curves of the pre-NP and pre-NZP products (Fig. S2, ESI†). The appropriate phosphatization temperature for the two precursors is preliminarily designed as 600 °C.

Fig. 1b comparatively displays the wide-angle X-ray diffraction (XRD) patterns of the NP MSs (the upper) and NZP HMSs (the lower) obtained at 600 °C for 2 h at a ramp rate of 3 °C min^{-1} under a N_2 atmosphere. The discernable diffraction reflections of the NP MSs, regardless of the peak locations and intensities, match well with the standard spectrum of the

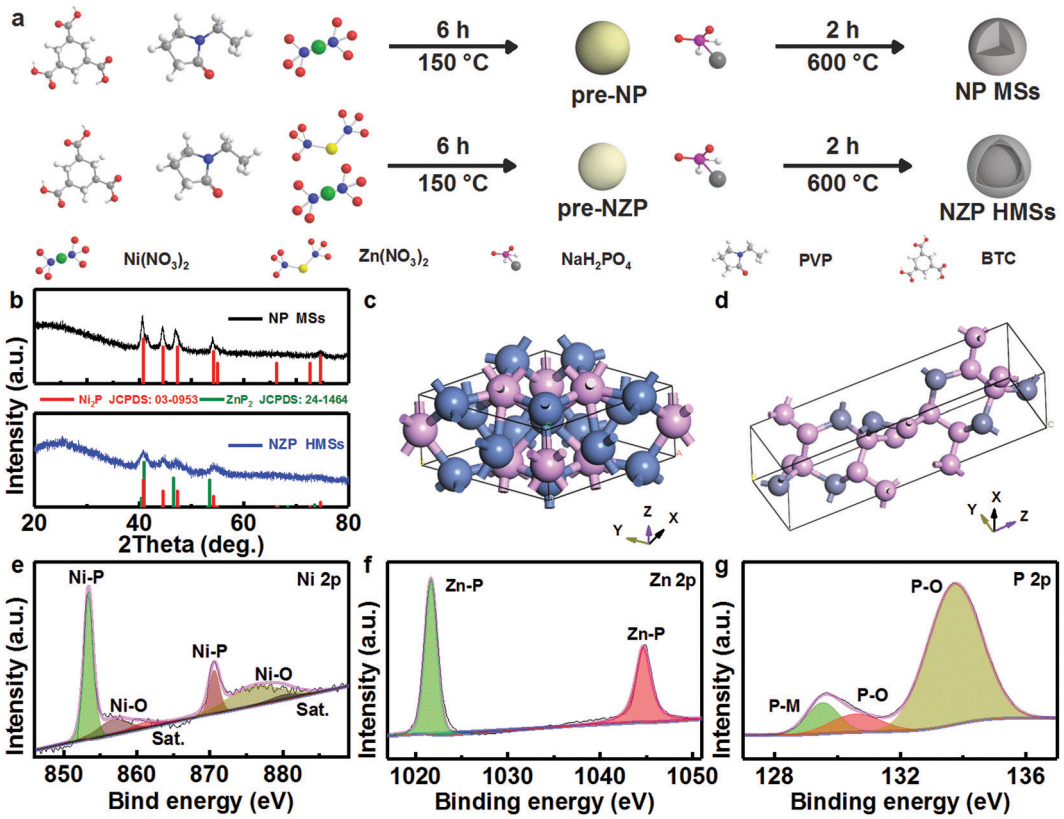

Fig. 1 (a) Schematic diagram of the synthesis procedure for the yolk–shell NZP HMSs and solid NP MSs. (b) XRD patterns of solid NP MSs and yolk–shell NZP HMSs. Crystallographic illustration of (c) hexagonal Ni_2P and (d) tetragonal ZnP_2. Typical XPS high-resolution elemental (e) Ni 2p, (f) Zn 2p and (g) P 2p spectra of the yolk–shell NZP HMSs.

hexagonal Ni_2P (JCPDS Card No. 03-0953) with a space group of *P*62*m* (189), where elemental Ni occupies the tetrahedral sites and the center hole sites surrounded by the tetrahedral atoms (Fig. 1c). By contrast, as for the NZP HMSs, all the diffraction peaks, can be unambiguously indexed to a mixture of hexagonal Ni_2P and tetragonal ZnP_2 (JCPDS Card No. 24-1464) with a space group of *P*43212 (96), in which the Zn and P occupy the center and vertex sites, respectively (Fig. 1d).

To further obtain the specific chemical states of Ni, Zn and P species on the surface of the NZP HMSs, X-ray photoelectron spectroscopy (XPS) analysis is conducted in detail, as depicted in Fig. 1e–g. Typical survey photoelectron spectrum shows the co-existence of Ni, Zn and P with a molar ratio of approximately 1 : 1 : 2.3 (Fig. S3, ESI†). The core level Ni 2p XPS spectra and the corresponding fitted data are illustrated in Fig. 1e. Evidently, the expected peaks of Ni-P bond are Ni $2p_{3/2}$ (~853.4 eV) and Ni $2p_{1/2}$ (~870.6 eV) along with two satellite (Sat.) peaks of ~861.0 and ~880.0 eV; another two peaks located at ~856.8 and ~876.0 eV are assigned to the Ni–O bond.[18,30] The high-resolution spectrum of Zn 2p (Fig. 1f) shows two peaks, corresponding to Zn $2P_{3/2}$ and Zn $2p_{1/2}$ located at binding energies (BEs) of ~1021.7 and ~1044.7 eV, respectively, and the BE gap of ~23.0 eV between the two peaks indicates the existence of the Zn–P bond.[31,32] As for the P 2p spectrum (Fig. 1g), the peaks centered at ~129.5 and ~130.6 eV are attributed to the P–M (M = Zn/Ni) bonds, confirming the presence of Ni_2P and ZnP_2,[33–36] and the peaks at BEs of ~133.2 and ~134.0 eV are assigned to typical P–O species from partially superficial oxidation.

Fig. 2a and b show the representative field-emission scanning electron microscopy (FESEM) and transmission electron microscopy (TEM) images of the resultant NP MSs. Obviously, lots of solid MSs with a smooth surface, well inheriting the typical morphology of pre-NP (Fig. S1a and b, ESI†), are characterized. The NZP HMS specimen shows a representative spherical architecture, similar to pre-NZP, but with numerous discernible nanoparticles of size ~10 nm located on their surface, rendering a rough surface. To visualize the nanoparticles more clearly, we purposefully chose the yolk–shell NZP-5 HMSs for further investigation. Apparently, the nanoparticles increase up to ~90 nm in size (Fig. S4a and b, ESI†), and can be confirmed to be the ZnP_2 phase with distinct elemental (Ni, Zn and P) distributions, as presented in STEM and the corresponding EDS mapping images (Fig. S4c, ESI†). Anyway, the sizes of both NP MSs and NZP HMSs are basically consistent with those of their precursors, indicating no occurrence of the distinct calcination-induced shrinkage. More interestingly, the NZP HMSs, unlike the NP MSs, manifest a yolk–shell structure with an apparent void, as verified by the sharp color contrast in Fig. 2e. And the shell is ~100 nm in thickness, along with a yolk of ~500 nm diameter. The higher magnification TEM (HRTEM) images (Fig. 2f and g) further corroborate the existence of nanoparticles on the rough surface of NZP HMSs. Further HRTEM observation (the inset in panel g) visualizes the well-defined lattice fringes

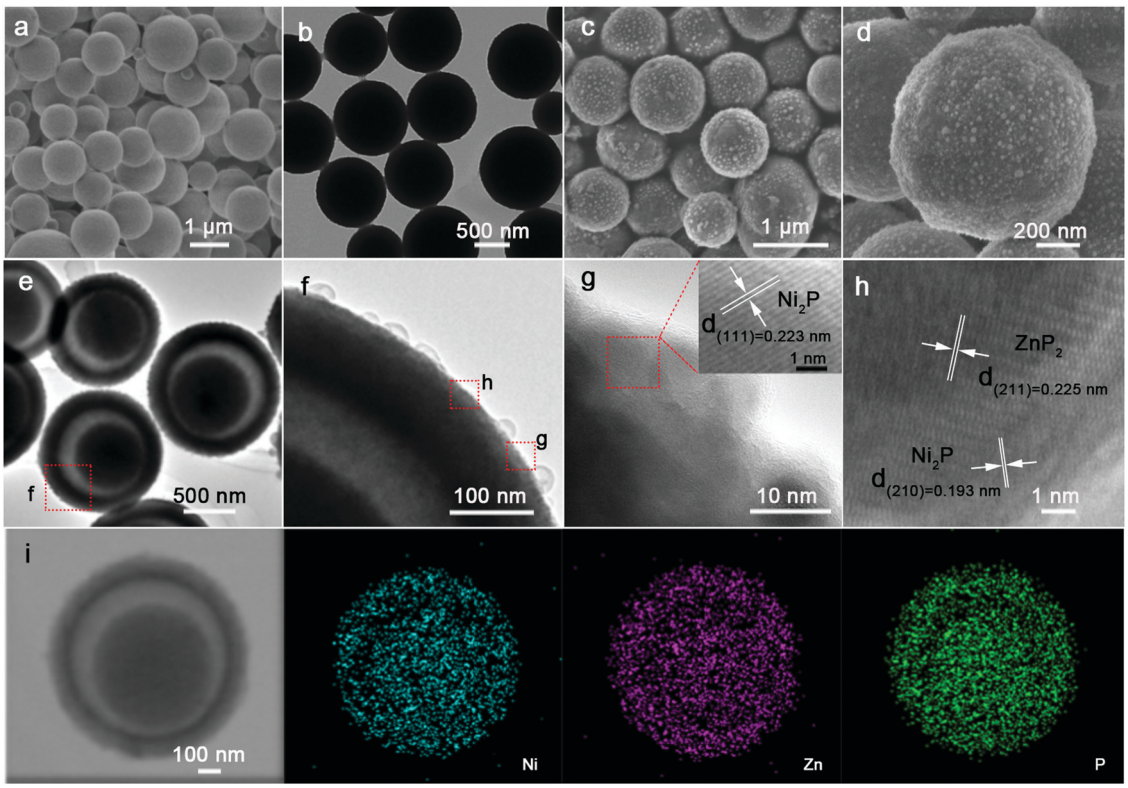

Fig. 2 (a) FESEM and (b) TEM images of the solid NP MSs. (c and d) FESEM, (e and f) TEM, (g and h) HRTEM, (i) STEM and corresponding elemental Ni, Zn and P mapping images of the yolk–shell NZP HMSs.

with a spacing of 0.223 nm, corresponding to the (111) crystalline plane of Ni_2P. Moreover, clear lattice fringes are evident in two regions with spacings of 0.193 and 0.225 nm, well indexed to the (210) plane of Ni_2P, and the (211) plane of ZnP_2, which authenticates that the nano-domains of Ni_2P and ZnP_2 are homogeneously dispersed with unique Ni_2P–ZnP_2 interfaces at the nanoscale, which can be well supported by the scanning TEM (STEM) and corresponding energy dispersive X-ray (EDX) elemental mapping images (Fig. 2i). Notably, the Ni, Zn and P species are all distributed perfectly throughout the whole yolk–shell sphere.

Corresponding N_2 sorption measurements (Fig. S5, ESI†) derive a Brunner–Emmett–Teller (BET) specific surface area (SSA) of $\sim$297.8 $m^2\ g^{-1}$ and pore volume of $\sim$0.7 $cm^3\ g^{-1}$ for the NZP HMSs, which are higher than those of their solid counterpart of NP MSs ($\sim$53.8 $m^2\ g^{-1}$ and $\sim$0.3 $cm^3\ g^{-1}$) and yolk–shell NZP-5 HMSs ($\sim$70.1 $m^2\ g^{-1}$ and $\sim$0.2 $cm^3\ g^{-1}$). It is the unique yolk–shell hollow architecture with hetero-interfaces at the nanoscale that will guarantee the large electrochemical active surface area (EASA) (*i.e.*, electrocatalyst/electrolyte contact area), enhanced charge transfer,[37] and lower chemisorption free energies of OH^-.[18] As a result, appealing electrocatalytic properties can be highly anticipated for the NZP HMS catalyst.

More interestingly, owing to the absence or introduction of extra elemental Zn, two distinguished structures, *i.e.*, solid NP MSs and yolk–shell NZP HMSs, are presented, while other synthetic parameters are always kept the same, as discussed above. It is worth mentioning that the difference has no effect on the morphologies of their precursors, and both of them are solid MSs with a similar size (Fig. S1, ESI†). Additionally, with the huge increase in the Zn content, namely without the addition of Ni species, the ZOP HMSs can be formed, rather than the ZnP_2 phase (Fig. S6, ESI†). Conversely, with a slight decrease in the Zn content, the solid NZP MSs can be surprisingly formed (Fig. S7a and b, ESI†). It is therefore concluded that elemental Zn plays a decisive role in the formation of yolk–shell HMSs over the annealing process. More appealingly, the yolk–shell NP HMSs (Fig. S7c and d, ESI†) can also be obtained by using the mixed solvent (*i.e.*, 15 mL of DMF and 15 mL of absolute alcohol) instead of the single-component DMF. And the yolk–shell hollow spherical Co_2P/ZnP_2 samples (Fig. S8a and b, ESI†) are still formed just by replacing the Ni species with elemental Co. Anyway, an in-depth exploration of the intrinsic role or the underlying formation mechanism of the yolk–shell hollow architecture is currently underway in our lab.

3.3 Electrochemical evaluation of the OER

Considering the appealing structural merits, as mentioned above, next, we mainly focus on the dependence of the OER performance of the resultant NZP HMS product upon their specific structures and composition. Accordingly, the OER catalytic activities of the yolk–shell NZP HMSs and solid NP MSs are systematically investigated in 1 M KOH aqueous solution as catalysts in a three-electrode cell. Remarkably, the

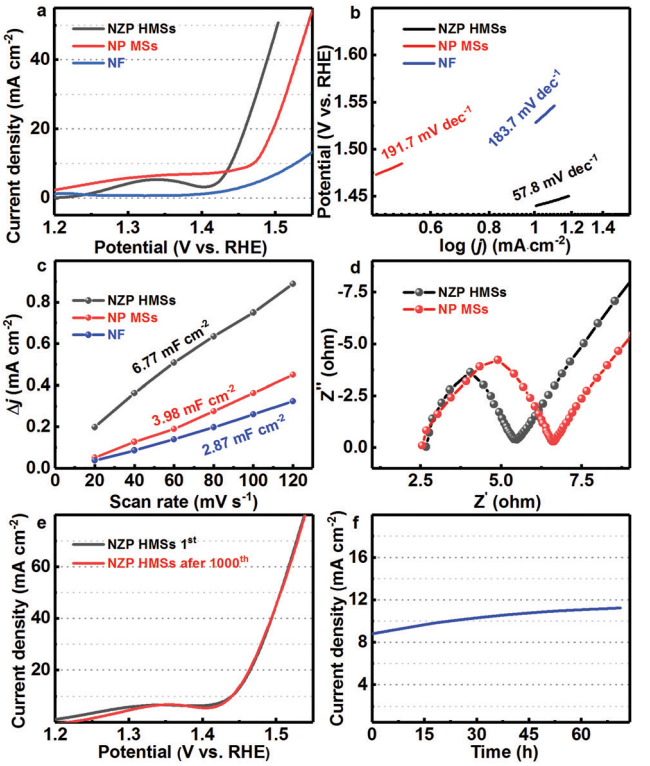

Fig. 3 (a) LSV curves, (b) Tafel slope plots, (c) capacitive currents as a function of scanning rates and (d) Nyquist plots of the yolk–shell NZP HMSs and NP MSs. (e) Polarization curves of the NZP HMS catalyst at its initial state and after 1000 cycles. (f) Long-term durability test plot with an overpotential of 210 mV.

yolk–shell NZP HMSs, as observed from the linear sweep voltammetry (LSV) curves (Fig. 3a), exhibit good catalytic performance, requiring a low overpotential of $\sim$210 mV to achieve a current density of 10 mA cm^{-2}, while the required overpotentials are $\sim$240 and $\sim$279 mV for the solid NP MSs and commercial NF support, respectively, to render the same current density. Considering that more ZnP_2 nanoparticles are located on the surface of yolk–shell NZP-5 HMSs, the OER performance of the yolk–shell NZP-5 HMSs is investigated with a low overpotential of $\sim$220 mV at 10 mA cm^{-2} (Fig. S9a, ESI†), which suggests that the large nanoparticles will decrease the OER properties, due to the increase in ZnP_2 content on the surface. Meanwhile, the solid NZP MSs and yolk–shell NP HMSs also present poor OER behaviors with low overpotentials of $\sim$243 and $\sim$263 mV at 10 mA cm^{-2}, respectively, although they are both better than the ZOP HMSs (a high overpotential of $\sim$398 mV at 2 mA cm^{-2}, Fig. S9a, ESI†). More encouragingly, the overpotential of the yolk–shell NZP HMSs is much lower than those of other reported Ni-based phosphide electrocatalysts ($\sim$240 to $\sim$360 mV) (Table S1, ESI†). Furthermore, the catalytic kinetics of the electrocatalysts are also evaluated by the Tafel slopes, as plotted in Fig. 3b. In general, a lower Tafel slope indicates higher electrocatalytic kinetics in the OER.[37] The Tafel slope of yolk–shell NZP HMSs, as displayed in Fig. 3b, is fitted as $\sim$57.8 mV dec^{-1}, which is much lower than those of the solid NP MS catalyst ($\sim$191.7 mV dec^{-1}), NF ($\sim$183.7 mV dec^{-1}),

yolk–shell NZP-5 HMSs (~94.7 mV dec^{-1}, Fig. S9b, ESI†), solid NZP MSs (~89.8 mV dec^{-1}) and yolk–shell NP HMSs (~93.4 mV dec^{-1}, Fig. S9b, ESI†), and even other retrieved Ni-based phosphides (~59–~153 mV dec^{-1}) (Table S1, ESI†), revealing that the NZP HMS catalyst possesses a favorable reaction kinetics toward the OER. More remarkably, both the lower overpotential and Tafel slope of the NZP HMSs observed here, to a great extent, highlight their distinct merits of the yolk–shell hollow structure and hetero Ni_2P–ZnP_2 interface towards the OER, since ZnP_2 is a fully inert phase in the OER.[38] To further assess the intrinsic catalytic activity of solid NP MSs and NZP HMSs, the TOFs are further analyzed at an overpotential of 210 mV, assuming that all the Ni atoms are the catalytically active centers. The TOF of the NZP HMSs is calculated as ~0.08 s^{-1}, which is higher than those of the NP MSs (~0.02 s^{-1}) and the NZP-5 HMSs (~0.06 s^{-1}).

As well established, the EASA, which always can be quantified by the double layer capacitance (C_{dl}), is another significant parameter affecting the catalytic performance of any electrocatalyst.[39] According to the cyclic voltammetry (CV) profiles (Fig. S10, ESI†) and scanning rate dependence of the current densities (Fig. 3c), the C_{dl} values of the NZP HMSs, NP MSs and NF are estimated as ~6.77, ~3.98 and ~2.87 mF cm^{-2}, respectively, elucidating that the yolk–shell hollow NZP HMSs possess more active surface area (~112.8 cm^2) compared with the NP MSs (~66.3 cm^2) and NF (~47.8 cm^2). The electrochemical impedance spectroscopy (EIS) plots of the NZP HMSs and NP MSs are depicted in Fig. 3d. And the NZP HMS catalyst exhibits a much smaller charge transfer resistance (R_{ct}) compared to the NP MSs, suggesting a fast electron transfer rate in the yolk–shell HMSs towards a highly efficient OER.[40] Besides the contribution from hollow, porous and yolk–shell structural features, the ZnP_2 phase enhanced the EASA and smaller R_{ct} observed in NZP HMSs cannot be ignored at all. Although ZnP_2 itself has no catalytic activity in the OER, it favors the enhancement of EASA, and rapid electronic transport owing to the rich hetero Ni_2P–ZnP_2 interfaces in the HMSs.

To identify the durability of the yolk–shell NZP HMS catalyst, continuous CV sweeps are performed from 1.2 to 1.6 V (*vs.* RHE) at a scanning rate of 100 mV s^{-1} in 1 M KOH aqueous solution. Impressively, no obvious change between the first and 1000th cycle can be detected in the LSV plot (Fig. 3e). Surprisingly, the current density in consecutive chronoamperometric tests first

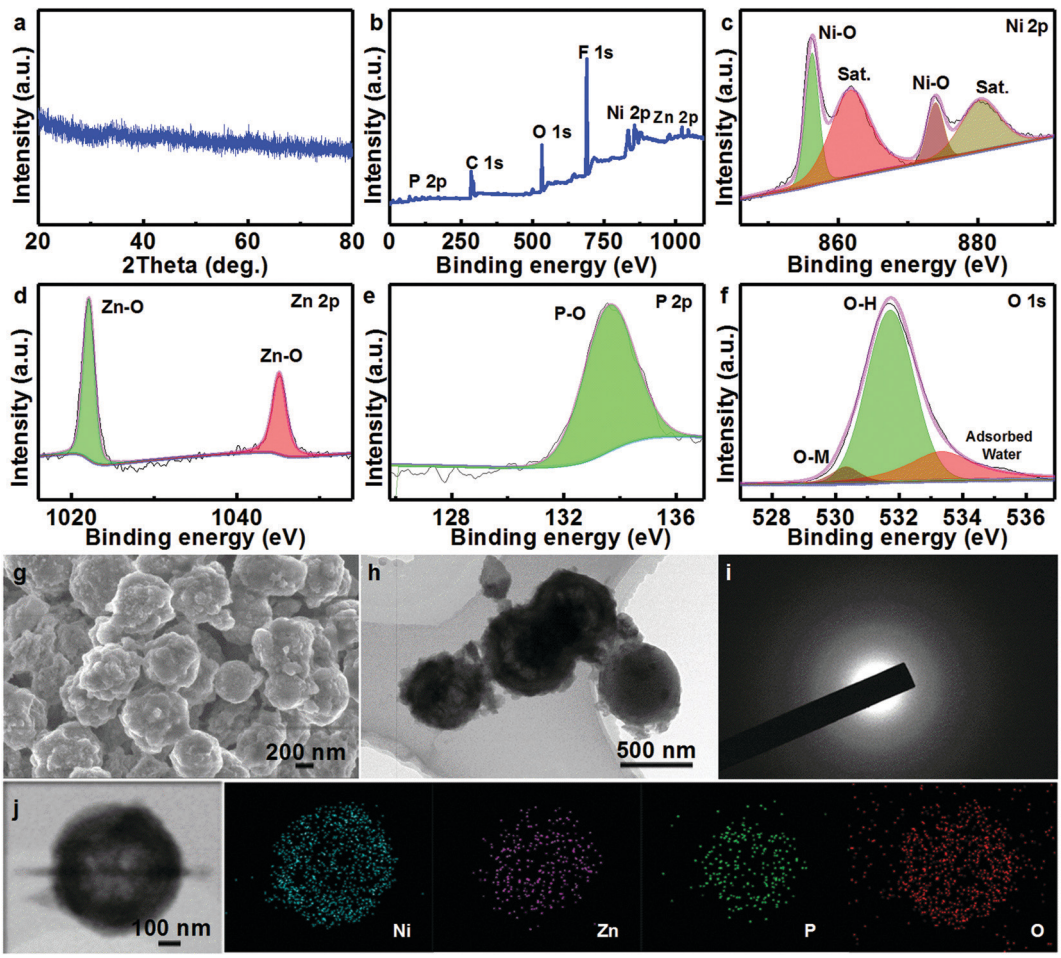

Fig. 4 Microstructure characterizations of the yolk–shell NZP HMSs after long-term durability test. (a) XRD pattern; XPS spectra for (b) survey pattern, (c) Ni 2p, (d) Zn 2p, (e) P 2p and (f) O 1s; (g) FESEM image; (h) TEM image; (i) SAED pattern; (j) STEM and corresponding elemental Ni, Zn, P and O mapping images.

increases, and afterward turns out to be relatively steady over 71 h at an overpotential of 210 mV (Fig. 3f), which highlights the superb electrochemical durability of yolk–shell NZP HMSs for OER application. Unlike other Ni-based phosphide electrocatalysts reported previously,[33,41] one abnormal phenomenon, that is the gradual increase in current density with testing, takes place in the yolk–shell NZP HMSs here, which suggests that something must have happened in the process.

To further understand the structural/compositional transformation of the NZP HMSs occurring over the long-term durability test in depth, XRD measurements are first conducted (Fig. 4a). Impressively, all the typical diffraction reflections of Ni_2P and ZnP_2 completely vanish, and new weak signals appear, and should be ascribed to the contribution from the as-formed $NiOOH/Zn(OH)_2$.[42] To support the statement, the surface element composition and chemical states of the cycled NZP HMSs are investigated by the XPS technique, as collected in Fig. 4b–f. As derived from the survey spectrum, elemental P and Zn become even less, and just about 3.6 and 3.5 at% can be detected, when compared to the fresh NZP HMSs (Fig. S3, ESI†). With regard to the Ni species (Fig. 4c), the two main peaks at ~856.2 and ~873.8 eV with a spin energy separation of ~17.6 eV correspond to Ni $2p_{3/2}$ and Ni $2p_{1/2}$, along with two Sat. peaks at ~880.2 and ~861.6 eV in the Ni 2p region, suggesting the presence of Ni^{3+} on the surface.[6,43] Additionally, the BEs for the Zn $2p_{3/2}$ (~1022.1 eV) and Zn $2p_{1/2}$ (~1045.1 eV) peaks in the Zn 2p region (Fig. 4d) are around 0.6 eV lower than those of yolk–shell NZP HMSs, and close to that of $Zn(OH)_2$.[44] The corresponding O 1s spectrum is presented in Fig. 4e. The three fitted peaks at 529.9, 531.6 and 533.3 eV are attributed to the main metal (Ni/Zn)–oxygen component, the hydroxyls and surface-adsorbed water molecules.[16,45] As for the P 2p spectrum (Fig. 4f), the representative peaks of the M–P (M = Ni/Zn) metal species disappear, and only those P–O species with higher valence are left, which indicates the formation of the soluble phosphorus oxides.[46] As a result, the P content in the cycled NZP HMSs largely decreases. With the XRD and XPS analysis above, it is easy to conclude that the yolk–shell NZP HMSs are fully converted into yolk–shell $NiOOH/Zn(OH)_2$ HMSs, and only the amorphous NiOOH is the real electroactive phase delivering the high performance during the OER process.[42] The decrease of the Zn species should be attributed to the partial dissolution of the newly formed amphoteric $Zn(OH)_2$ into the 1 M KOH electrolyte. This will indeed increase the naked surface of the electroactive NiOOH for the OER, thus leading to the increase of the current density over testing (Fig. 3f). Although the changes in compositions/phases take place, the hollow yolk–shell spherical structure is basically retained (Fig. 4g and h). Further, the SAED pattern (Fig. 4i) of the yolk–shell NZP catalyst after a 71 h OER test shows gray and poorly constructive electron diffraction rings, corroborating its amorphous feature, which is in good agreement with the XRD analysis above (Fig. 4a). Further STEM and elemental mapping images (Fig. 4i) visualize the uniform distribution of Ni, Zn, P and O in the yolk–shell MSs, and low contents of Zn and P, while a high proportion of O species in the unique structure.

4. Conclusions

In summary, we first synthesized yolk–shell Ni_2P/ZnP_2 hollow microspheres (NZP HMSs) through simple phosphatization of a bimetallic organic framework precursor, and further used them as a high-performance electrocatalyst for the OER. The heterophase ZnP_2 by itself was electrochemically inert in the OER, but it favored the improvement in electroactive surface area and rapid charge transport, thanks to the rich hetero Ni_2P–ZnP_2 interfaces in unique yolk–shell NZP HMSs. The as-fabricated yolk–shell NZP HMSs displayed more excellent OER properties in terms of overpotentials, catalytic kinetics, and stabilities than the solid Ni_2P microspheres in 1 M KOH, benefiting from their remarkable structural and compositional merits. Our contribution here may inspire a constructive way to synthesize other yolk–shell hollow transition metal phosphides with hetero-interfaces toward energy conversion applications and beyond.

Conflicts of interest

There are no conflicts to declare.

Acknowledgements

The authors acknowledge the financial support from the National Natural Science Foundation of China (No. 51772127, 51772131), Taishan Scholars (No. ts201712050), the Major Program of Shandong Province Natural Science Foundation (ZR2018ZB0317) and the Collaborative Innovation Center of Technology and Equipment for Biological Diagnosis and Therapy in Universities of Shandong.

References

1 H. J. Yan, Y. Xie, A. P. Wu, Z. C. Cai, L. Wang, C. G. Tian, X. M. Zhang and H. G. Fu, Anion-modulated HER and OER activities of 3D Ni-V-based interstitial compound heterojunctions for high-efficiency and stable overall water splitting, *Adv. Mater.*, 2019, **31**, 1901174.

2 L. A. Stern, L. Feng, F. Song and X. Hu, Ni_2P as a Janus catalyst for water splitting: the oxygen evolution activity of Ni_2P nanoparticles, *Energy Environ. Sci.*, 2015, **8**, 2347.

3 B. Chi, H. Lin and J. B. Li, Cations distribution of $Cu_xCo_{3-x}O_4$ and its electrocatalytic activities for oxygen evolution reaction, *Int. J. Hydrogen Energy*, 2008, **33**, 4763.

4 X. M. Bu, R. J. Wei, W. Gao, C. Y. Lan and J. C. Ho, A unique sandwich structure of a CoMnP/Ni_2P/NiFe electrocatalyst for highly efficient overall water splitting, *J. Mater. Chem. A*, 2019, **7**, 12325.

5 X. Liu, Y. Yuan, J. Liu, B. Liu, X. Chen, J. Ding, X. Han, Y. Deng, C. Zhong and W. Hu, Utilizing solar energy to improve the oxygen evolution reaction kinetics in zinc-air battery, *Nat. Commun.*, 2019, **10**, 1.

6 H. M. Sun, X. B. Xu, Z. H. Yan, X. Chen, F. Y. Cheng, P. S. Weiss and J. Chen, Porous multishelled Ni_2P hollow

microspheres as an active electrocatalyst for hydrogen and oxygen evolution, *Chem. Mater.*, 2017, **29**, 8539.

7 S. Anantharaj, P. E. Karthik and S. Kundu, Self-assembled IrO_2 nanoparticles on a DNA scaffold with enhanced catalytic and oxygen evolution reaction (OER) activities, *J. Mater. Chem.*, 2015, **3**, 24463.

8 S. M. Galani, A. Mondal, D. N. Srivastava and A. B. Panda, Development of RuO_2/CeO_2 heterostructure as an efficient OER electrocatalyst for alkaline water splitting, *Int. J. Hydrogen Energy*, 2019, DOI: 10.1016/j.ijhydene.2019.08.026.

9 T. Weber, T. Ortmann, D. Escalera-López, M. J. Abb, B. Mogwitz, S. Cherevko, M. Rohnke and H. Over, Visualizing potential-induced pitting corrosion of ultrathin single-crystalline IrO_2 (110) films on RuO_2 (110)/Ru (0001) under electrochemical water splitting conditions, *ChemCatChem*, 2019, **11**, 1.

10 L. Y. Zeng, K. A. Sun, X. B. Wang, Y. Q. Liu, Y. Pan, Z. Liu, D. W. Cao, Y. Song, S. H. Liu and C. G. Liu, Three–dimensional–networked Ni_2P/Ni_3S_2 heteronanoflake arrays for highly enhanced electrochemical overall-water-splitting activity, *Nano Energy*, 2018, **51**, 26.

11 X. Xing, R. Liu, K. Cao, U. Kaiser and C. Streb, Transition metal oxides/carbides@carbon nanotube composites as multifunctional electrocatalysts for challenging oxidations and reductions, *Chem. – Eur. J.*, 2019, **25**, 11098.

12 W. Li, D. H. Xiong, X. F. Gao and L. F. Liu, The oxygen evolution reaction enabled by transition metal phosphide and chalcogenide pre-catalysts with dynamic changes, *Chem. Commun.*, 2019, **55**, 8744.

13 J. M. V. Nsanzimana, L. Q. Gong, R. Dangol, V. Reddu, V. Jose, B. Y. Xia, Q. Y. Yan, J. M. Lee and X. Wang, Tailoring of metal boride morphology via anion for efficient water oxidation, *Adv. Eng. Mater.*, 2019, **9**, 1901503.

14 X. Peng, C. Pi, X. Zhang, S. Li, K. Huo and P. K. Chu, Recent progress of transition metal nitrides for efficient electrocatalytic water splitting, *Sustainable Energy Fuels*, 2019, **3**, 366.

15 M. Ju, X. Wang, X. Long and S. Yang, Recent advances in transition metal based compound catalysts for water splitting from the perspective of crystal engineering, *CrystEngComm*, 2020, **22**, 1531.

16 H. Q. Zhou, F. Yu, J. Y. Sun, R. He, S. Chen, C. W. Chu and Z. F. Ren, Highly active catalyst derived from a 3D foam of $Fe(PO_3)_2/Ni_2P$ for extremely efficient water oxidation, *Proc. Natl. Acad. Sci. U. S. A.*, 2017, **114**, 5607.

17 H. Li, Y. Du, Y. Fu, C. Wu, Z. Xiao, Y. Liu, X. Sun and L. Wang, Self-supported Ni_2P nanotubes coated with FeP nanoparticles electrocatalyst (FeP@Ni_2P/NF) for oxygen evolution reaction, *Int. J. Hydrogen Energy*, 2020, **45**, 565.

18 Y. T. Yan, J. H. Lin, K. Bao, T. X. Xu, J. L. Qi, J. Cao, Z. X. Zhong, W. D. Fei and J. C. Feng, Free–standing porous Ni_2P–Ni_5P_4 heterostructured arrays for efficient electrocatalytic water splitting, *J. Colloid Interface Sci.*, 2019, **552**, 332.

19 P. Y. Wang, Z. H. Pu, W. Q. Li, J. W. Zhu, C. T. Zhang, Y. F. Zhao and S. C. Mu, Coupling $NiSe_2$–Ni_2P heterostructure nanowrinkles for highly efficient overall water splitting, *J. Catal.*, 2019, **377**, 600.

20 J. Y. Wang, J. W. Wan, N. L. Yang, Q. Li and D. Wang, Hollow multishell structures exercise temporal–spatial ordering and dynamic smart behaviour, *Nat. Rev. Chem.*, 2020, **4**, 159.

21 J. Y. Wang, J. W. Wan and D. Wang, Hollow multishelled structures for promising applications: understanding the structure–performance correlation, *Acc. Chem. Res.*, 2019, **52**, 2169.

22 J. Zhang, J. W. Wan, J. Y. Wang, H. Ren, R. B. Yu, L. Gu, Y. L. Liu, S. H. Feng and D. Wang, Hollow multi-shelled structure with metal–organic–framework–derived coatings for enhanced lithium storage, *Angew. Chem., Int. Ed.*, 2019, **58**, 5266.

23 L. Wang, J. W. Wan, Y. S. Zhao, N. L. Yang and D. Wang, Hollow multi-shelled structures of Co_3O_4 dodecahedron with unique crystal orientation for enhanced photocatalytic CO_2 reduction, *J. Am. Chem. Soc.*, 2019, **141**, 2238.

24 C. W. Jiao, Z. M. Wang, X. X. Zhao, H. Wang, J. Wang, R. B. Yu and D. Wang, Triple-shelled manganese–cobalt oxide hollow dodecahedra with highly enhanced performance for rechargeable alkaline batteries, *Angew. Chem., Int. Ed.*, 2019, **58**, 996.

25 D. Mao, J. W. Wan, J. Y. Wang and D. Wang, Sequential templating approach: a groundbreaking strategy to create hollow multishelled structures, *Adv. Mater.*, 2019, **31**, 1802874.

26 H. W. Liang, X. D. Zhuang, S. Brüller, X. L. Feng and K. Müllen, Hierarchically porous carbons with optimized nitrogen doping as highly active electrocatalysts for oxygen reduction, *Nat. Commun.*, 2014, **5**, 1.

27 X. P. Han, F. Y. Cheng, T. R. Zhang, J. G. Yang, Y. X. Hu and J. Chen, Hydrogenated uniform Pt clusters supported on porous $CaMnO_3$ as a bifunctional electrocatalyst for enhanced oxygen reduction and evolution, *Adv. Mater.*, 2014, **26**, 2047.

28 M. Wang, M. Lin, J. Li, L. Huang, Z. Zhuang, C. Lin, L. Zhou and L. Mai, Metal-organic framework derived carbon–confined Ni_2P nanocrystals supported on graphene for an efficient oxygen evolution reaction, *Chem. Commun.*, 2017, **53**, 8372.

29 Z. L. Wang, D. K. Denis, Z. W. Zhao, X. Sun, J. Y. Zhang, L. R. Hou and C. Z. Yuan, Unusual formation of hollow $NiCoO_2$ sub–microspheres by oxygen functional group dominated thermally induced mass relocation towards efficient lithium storage, *J. Mater. Chem. A*, 2019, **7**, 18109.

30 C. F. Dong, L. J. Guo, Y. Y. He, C. J. Chen, Y. T. Qian, Y. N. Chen and L. Q. Xu, Sandwich–like Ni_2P nanoarray/nitrogen–doped graphene nanoarchitecture as a high–performance anode for sodium and lithium ion batteries, *Energy Storage Mater.*, 2018, **15**, 234.

31 M. C. Biesinger, L. W. M. Lau, A. R. Gerson and R. S. C. Smart, Resolving surface chemical states in XPS analysis of first row transition metals, oxides and hydroxides: Sc, Ti, V, Cu and Zn, *Appl. Surf. Sci.*, 2010, **257**, 887.

32 N. Kamarulzaman, M. F. Kasim and N. F. Chayed, Elucidation of the highest valence band and lowest conduction band shifts using XPS for ZnO and $Zn_{0.99}Cu_{0.01}O$ band gap changes, *Results Phys.*, 2016, **6**, 217.

33 X. Cheng, Z. Pan, C. Lei, Y. J. Jin and Y. Hou, Strongly coupled 3D ternary Fe_2O_3@Ni_2P/$Ni(PO_3)_2$ hybrid for enhanced

electrocatalytic oxygen evolution at ultra-high current densities, *J. Mater. Chem.*, 2019, **7**, 965.

34 Y. Li, Z. Jin, L. Zhang and K. Fan, Controllable design of Zn–Ni–P on g–C_3N_4 for efficient photocatalytic hydrogen production, *Chin. J. Catal.*, 2019, **40**, 390.

35 H. Gu, Y. Gu, Z. Li, Y. Ying and Y. Qian, Low–temperature route to nanoscale P_3N_5 hollow spheres, *J. Mater. Res.*, 2003, **18**, 2359.

36 Q. Guo, Q. Yang, Z. Lei, C. Yi and X. Yi, Large–scale synthesis of amorphous phosphorus nitride imide nanotubes with high luminescent properties, *J. Mater. Res.*, 2005, **20**, 325.

37 Z. X. Yin, C. L. Zhu, C. Y. Li, S. Zhang, X. T. Zhang and Y. J. Chen, Hierarchical nickel–cobalt phosphide yolk–shell spheres as highly active and stable bifunctional electrocatalysts for overall water splitting, *Nanoscale*, 2016, **8**, 19129.

38 H. Xu, P. P. Song, C. F. Liu, Y. P. Zhang and Y. K. Du, Facile construction of ultrafine nickel–zinc oxyphosphide nanosheets as high–performance electrocatalysts for oxygen evolution reaction, *J. Colloid Interface Sci.*, 2018, **530**, 58.

39 S. Sun, H. Li and Z. J. Xu, Impact of surface area in evaluation of catalyst activity, *Joule*, 2018, **2**, 1.

40 A. P. Murthy, J. Theerthagiri, J. Madhavan and K. Murugan, Highly active MoS_2/carbon electrocatalysts for the hydrogen evolution reaction-insight into the effect of the internal resistance and roughness factor on the Tafel slope, *Phys. Chem. Chem. Phys.*, 2017, **19**, 1988.

41 X. G. Wang, W. Li, D. H. Xiong, D. Y. Petrovykh and L. F. Liu, Bifunctional nickel phosphide nanocatalysts supported on carbon fiber paper for highly efficient and stable overall water splitting, *Adv. Funct. Mater.*, 2016, **26**, 4067.

42 H. D. Hosseini and S. Shahrokhian, Self-supported nanoporous Zn–Ni–Co/Cu selenides microball arrays for hybrid energy storage and electrocatalytic water/urea splitting, *Chem. Eng. J.*, 2019, **375**, 122090.

43 A. Nadeema, V. M. Dhavale and S. Kurungot, NiZn double hydroxide nanosheet-anchored nitrogen-doped graphene enriched with the γ-NiOOH phase as an activity modulated water oxidation electrocatalyst, *Nanoscale*, 2017, **9**, 12590.

44 J. Winiarski, W. Tylus, K. Winiarska, I. Szczygieł and B. Szczygieł., XPS and FT-IR characterization of selected synthetic corrosion products of zinc expected in neutral environment containing chloride ions, *J. Spectrosc.*, 2018, **2018**, 1.

45 L. R. Hou, Y. Y. Shi, C. Wu, Y. R. Zhang, Y. Z. Ma, X. Sun, J. F. Sun, X. G. Zhang and C. Z. Yuan, Monodisperse metallic $NiCoSe_2$ hollow sub-microspheres: Formation process, intrinsic charge-storage mechanism, and appealing pseudocapacitance as highly conductive electrode for electrochemical supercapacitors, *Adv. Funct. Mater.*, 2018, **28**, 1705921.

46 Q. Guo, Q. Yang, L. Zhu, C. Yi and Y. Xie, Large-scale synthesis of amorphous phosphorus nitride imide nanotubes with high luminescent properties, *J. Mater. Res.*, 2011, **20**, 325.

